Magnetic force microscopy signatures of higher-order skyrmions and antiskyrmions

Sabri Koraltan, Joe Sunny, Tamer Karaman, Reshma Peremadathil Pradeep, Emily Darwin, Felix Büttner, Dieter Suess, Hans Josef Hug, Manfred Albrecht

Angaben zur Veröffentlichung / Publication details:

Koraltan, Sabri, Joe Sunny, Tamer Karaman, Reshma Peremadathil Pradeep, Emily Darwin, Felix Büttner, Dieter Suess, Hans Josef Hug, and Manfred Albrecht. 2026. "Magnetic force microscopy signatures of higher-order skyrmions and antiskyrmions." *Advanced Functional Materials* 36 (41): e25716. https://doi.org/10.1002/adfm.202525716.

Advanced Functional Materials

ADVANCED FUNCTIONAL MATERIALS
www.afm-journal.de

RESEARCH ARTICLE OPEN ACCESS

Magnetic Force Microscopy Signatures of Higher-Order Skyrmions and Antiskyrmions

Sabri Koraltan[1,2,3,4,5] | Joe Sunny[5] | Tamer Karaman[5] | Reshma Peremadathil-Pradeep[6,7] | Emily Darwin[6] | Felix Büttner[5,8] | Dieter Suess[2,3] | Hans Josef Hug[6,7] | Manfred Albrecht[5]

[1]Institute of Applied Physics, TU Wien, Vienna, Austria | [2]Physics of Functional Materials, Faculty of Physics, University of Vienna, Vienna, Austria | [3]Research Platform MMM Mathematics-Magnetism-Materials, University of Vienna, Vienna, Austria | [4]Vienna Doctoral School in Physics, University of Vienna, Vienna, Austria | [5]Institute of Physics, University of Augsburg, Augsburg, Germany | [6]Magnetic & Functional Thin Films Laboratory, Empa, Swiss Federal Laboratories for Materials Science and Technology, Ueberlandstrasse 129, Dübendorf, Switzerland | [7]Department of Physics, University of Basel, Basel, Switzerland | [8]Helmholtz-Zentrum Berlin, Berlin, Germany

Correspondence: Sabri Koraltan (sabri.koraltan@tuwien.ac.at)

Received: 26 September 2025 | **Revised:** 16 January 2026 | **Accepted:** 23 February 2026

Keywords: higher-order skyrmions | magnetic force microscopy | skyrmions

ABSTRACT

Higher-order skyrmions and antiskyrmions are topologically protected spin textures with integer topological charges beyond ±1, typically nucleating from vertical Bloch lines in domain walls. Until now, they have been reported only in ferromagnetic multilayers by Lorentz transmission electron microscopy (LTEM), which requires growth on ultrathin membranes and complicates their integration into spintronic devices. Moreover, LTEM often yields contrast patterns that are difficult to unambiguously assign to specific topological charges. Here, we demonstrate that magnetic force microscopy (MFM) operated under vacuum conditions provides a robust route to identify and distinguish higher-order spin textures in Co/Ni multilayers at room temperature. Supported by micromagnetic simulations, we show that MFM can resolve vertical Bloch lines as well as skyrmions and antiskyrmions with arbitrary charge. Our results establish advanced MFM as a powerful technique for the qualitative classification of complex spin textures, paving the way for their exploration and utilization in future skyrmionic device concepts.

1 | Introduction

Nonuniform magnetization configurations have been envisioned to be useful in a wide variety of technological applications, ranging from magnetic vortices for magnetic field sensors [1, 2] to domain wall-based race track memories [3] or logical devices [4–6]. Considering the nonuniform 1D textures of the domain walls, they were desirable for spintronic devices because of their ability to control them with external fields and electrical currents [7]. Later, 2D spin textures known as magnetic skyrmions gained popularity [8, 9]. Skyrmions are topologically nontrivial spin objects. Their annihilation into a trivial magnetic state (e.g., a uniformly magnetized state) often requires overcoming a significant energy barrier. This barrier might arise because changing the topological winding number Q could involve singularities (discontinuities) in the magnetization field, which are energetically costly. Because the skyrmions can be stable under external magnetic fields at ambient temperature in specific materials, and they can be set into motion by electric currents and temperature gradients, they have been proposed to be used in skyrmion racetrack memory devices [10–12] or for reservoir and unconventional computing tasks [13–16]. With the discovery of their topological counterparts, the antiskyrmions, improved schemes for skyrmion and antiskyrmion-based memory devices have been proposed [17]. A

key challenge here is to find a suitable material in which both objects can co-exist. So far, this has only been observed in a handful of materials such as non-centrosymmetric Heussler compounds [18–20], chiral bulk magnet FeGe [21], and ferrimagnetic multilayers [22]. For applications such as reservoir computing where the skyrmionic materials act as the reservoir fabric and the spin objects are excited by high-frequency alternating currents or fields, it would be beneficial to use a high number of distinct spin objects with similar properties to increase the level of nonlinearity in the system. It was shown that materials exist where skyrmions with topological numbers (Q) other than one can be stabilized in the form of skyrmion bags and bundles using chiral magnets, which are stable at low temperatures [23–25] and room temperature [26]. In this regard, hard magnetic bubbles were studied in the early 1970s [27, 28], which, from the present perspective, appear to have topological charges different from one. There exists even a (single) transmission electron micrograph image [29], which appears to have an experimental proof of a hard magnetic bubble.

Recently, we have experimentally demonstrated that skyrmions and antiskyrmions with arbitrary topological charge are intrinsically stable in ferromagnetic Co/Ni multilayers [30]. The near-compensation of the positive perpendicular anisotropy and the negative shape anisotropy energy densities allows the formation of 0D topological defects inside regular Bloch-type domain walls (Figure 1a), known as vertical Bloch lines (vBL). The spin configuration of a vBL is depicted, for example, in Figure 1b. When subjected to an out-of-plane (oop) magnetic field, the domain walls and vBL's shrink and distinct spin textures form such as skyrmions, antiskyrmions, trivial bubbles, as well as higher-order skyrmions and antiskyrmions. In panel I. of Figure 1c–h, we provide an overview of different spin textures that can be stabilized in Co/Ni-based ferromagnetic multilayers. So far, they have only been observed using Lorentz transmission electron microscopy (LTEM), which requires the multilayer to be deposited on an electron-transparent Si_3N_4 membrane. Samples thus have to be specially prepared for a successive LTEM study, and the preparation on a thin membrane limits heat dissipation, making it challenging to study devices with imposed currents. Furthermore, there are debates about the image formation mechanisms involved in LTEM [31], which could lead to similar, if not identical, contrasts for different spin textures, as is the case for biskyrmions and trivial bubbles [32–35]. It is noteworthy that other imaging techniques can be employed to unambiguously identify spin-textures, such as X-ray tomography with ptychography [36] or holography [37], and quantum sensors [38], which might bring different complications and limitations.

In this work, we show that topologically different spin textures such as skyrmions, biskyrmions, antiskyrmions, and further higher-order spin textures can be mapped uniquely by a magnetic force microscope operated under vacuum conditions [39]. First, we discuss the anatomy of MFM contrasts by employing state-of-the-art micromagnetic simulations, and provide an overview about the MFM signatures of higher-order skyrmions and antiskyrmions. We experimentally verify our numerical results by using a Co/Ni multilayer grown by DC magnetron sputtering. After confirming the type of skyrmionic textures present in the stack by means of LTEM, we show that vBLs, as well as spin objects with higher topological charge can be observed using MFM under vacuum conditions. Our experiments demonstrate that MFM permits the identification and discrimination of the various spin objects and can potentially be used to study future skyrmionic devices utilizing higher-order spin textures with arbitrary topological charge.

2 | Results

2.1 | MFM Signatures of Single Spin-Objects

To better understand the expected MFM contrasts, we performed micromagnetic simulations using the finite-difference-based python package `magnum.np` [40], as described in detail in Methods. Here, we use ideal material parameters from our previous work [30] to reliably stabilize higher-order spin-textures with $Q \in [-10, 10]$.

The MFM contrasts of the magnetization states shown in panel II. of Figure 1c–h are depicted assuming $\boldsymbol{\mu}_{\text{tip}} = (0, 0, 1 \times 10^{-16}\,\text{Am}^{-2})$. A closer look at Figure 1c,II reveals that two main contrasts are visible on the white background: a red contrast, which occurs because of an attractive force between the tip and magnetization, and a blue contrast, which occurs because of the repulsive force around the skyrmion with $Q = -1$. The gray arrows are a guide for the eye to understand the magnetization of the sample and help to determine the localization of the contrasts. In this case, the magnetization does not show any divergences but is in a flux closure state: a Bloch skyrmion. Here, the shadow contrast is present all around the spin object. When considering an antiskyrmion with $Q = +1$, as shown in Figure 1(d,II), we observe that the magnetization shows two Néel segments in addition to the Bloch walls [18]. In this case, the magnetization shows head-to-head spins along the horizontal segment and tail-to-tail spins along the transversal segment. This leads to a clear localization of the MFM contrast, where the now rather elliptical core shows a strong attractive signal, and is accompanied by two repulsive lobes of shadow contrasts localized at the head-to-head spin configurations (yellow dashed circle), while the tail-to-tail spins show no additional MFM contrast (purple dashed circle). We continue the analysis with the visual inspection of the MFM contrast of a $Q = 0$ bubble, which reveals that a kink in the magnetization, where the spins diverge from a common spot (tail-to-tail), generates no significant stray field, while a kink in the magnetization, where spins are opposing each other in a common spot (head-to-head), a significant increase in the stray field is observed, leading to a strong MFM contrast.

Combining the results from these three objects, we observe that the local spin configuration can either lead to an enhancement of the stray-field, and thus a strong MFM contrast surrounded by a shadow contrast which is of opposing force, or a diminishment of the stray-fields which results in kinks in the shadow contrast as well as localization of the MFM contrast. This holds also for other spin objects such as $Q = -2$ (Figure 1f), $Q = -5$ (Figure 1g), and $Q = -5$ (Figure 1h), respectively.

As expected, the situation changes slightly when the diameter of the spin objects increases with the higher-order skyrmions and antiskyrmions. Now, the cores of the spin textures are larger, and

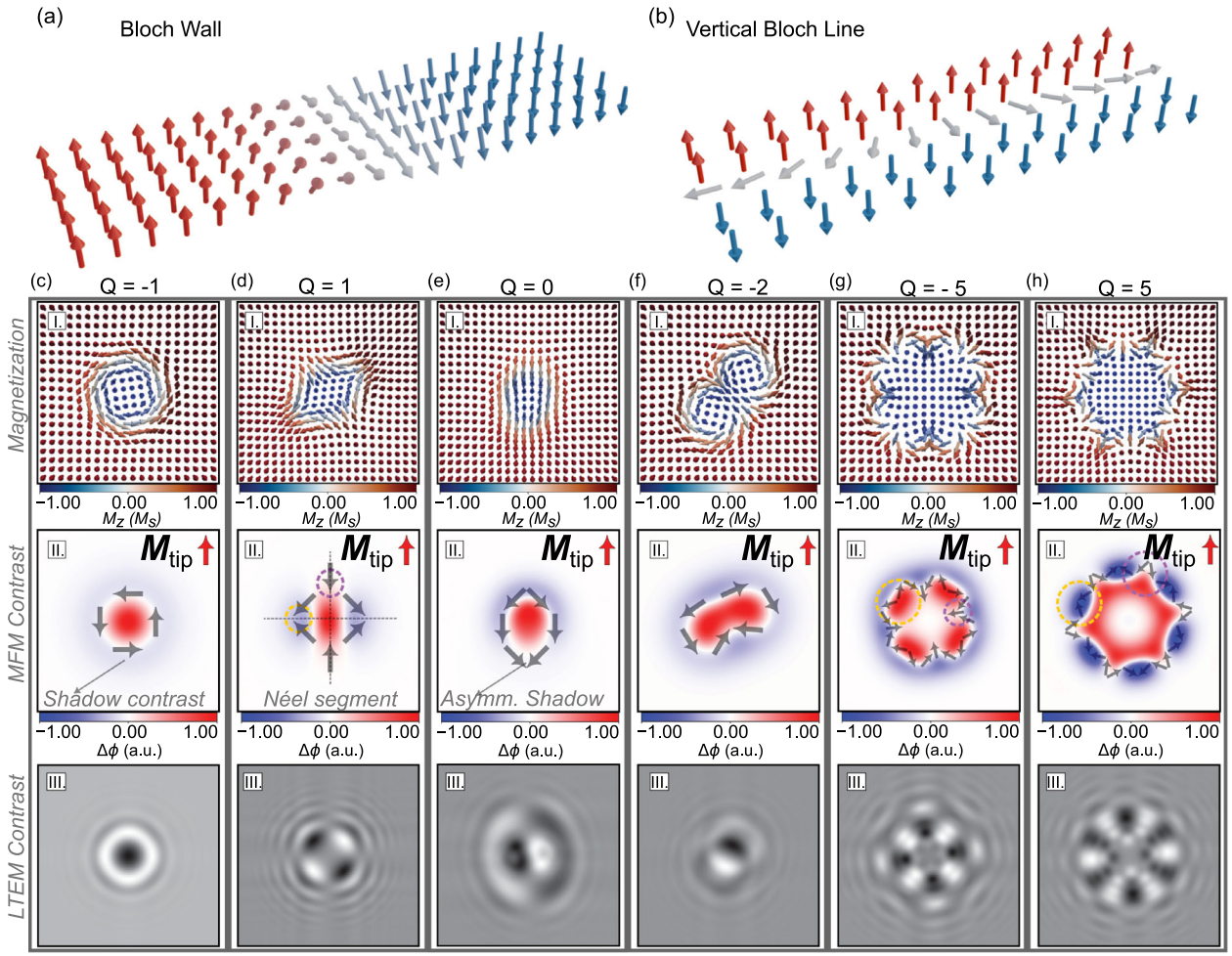

FIGURE 1 | Overview of spin objects and contrasts mechanisms. Schematic illustration of the magnetization configuration of a conventional Bloch wall in (a), of a topological defect known as vertical Bloch line in (b), a $Q = -1$ Bloch skyrmion in (c), a $Q = +1$ antiskyrmion in (d), a $Q = 0$ trivial bubble in (e), a $Q = -2$ biskyrmion in (f), a $Q = -5$ higher-order skyrmion in (g), and of a $Q = +5$ higher-order antiskyrmion in (h), respectively. In each subfigure we show three panels: (I): magnetization vectors, where the color represents the normalized oop components, (II): simulated MFM contrasts, where the gray arrows are a guide to the eye to understand where the constrats sourcing from, and (III): simulated underfocus LTEM contrasts. The gray arrows in II. show the relavant magnetization vectors, while the purple circles show areas where the stray fields vanish localy, and the yellow dashed circles show a localized increased in the stray field.

their boundaries are well separated by the core; see Figure 1g,h. For a higher-order skyrmion with $Q = -5$, a strong localization of the attractive force inside the spin object (yellow dashed circle) is observed as the size of the kinks decreases while the total size of the spin object increases. The MFM contrasts rising from the head-to-head spins appears to interrupt the inner attractive signal leading to the localization of the four attractive (red) lobes inside the boundary where the tail-to-tail spins are present. Furthermore, a slight increase and localization of repulsive shadow contrast is observed at the head-to-head spins. The situation changes for a higher-order antiskyrmion (Figure 1h), where the head-to-head spins lead to a clearly enhanced and very localized repulsive contrasts (yellow dashed circle), and the tail-to-tail sections are not only interupting the shadow contrasts and help in the localization of the repulsive contrats, but these sections also lead to a localized increase of the attractive force inside the boundary of the spin object.

For the sake of completeness we provide in panel III of Figure 1c–h the simulated underfocused LTEM contrasts of the same spin objects. Typically, Bloch skyrmions (Figure 1c,III) can be well differentiated from other spin-objects. While antiskyrmions also appear to have a rather unique LTEM contrast (Figure 1d,III), it can be clearly seen that the contrasts for the $Q = 0$ bubble (Figure 1e,III) and the $Q = -2$ biskyrmion (Figure 1f,III) are quite similar. When the noise present in ultrathin ferro- or ferrimagnetic multilayers is considered alongside further noise sources in a real experimental setup, it can become rather challenging to distinguish between different spin objects. Furthermore, correct discrimination of spin objects becomes even more challenging with increasing Q. The $Q = -5$ skyrmion in Figure 1g,III has four dark and four bright regions and the $Q = +5$ skyrmion in Figure 1h,III has six dark and bright regions. As we also know from our previous work, the contrast of a $Q = -5$ might not be indifferentiable from the contrast of a $Q = +3$ object (not shown here).

In summary, our initial micromagnetic simulations reveal that, in contrast to LTEM, MFM is ideally able to deliver contrasts with key signatures that can be useful for a qualitative discrimination of spin textures with arbitrary topological charges. Here, we identify several key signatures that are different for higher-order skyrmions ($Q < 0$) and higher-order antiskyrmions ($Q > 0$). That is, higher-order skyrmions can be characterized by localized attractive lobes inside the boundaries, while maintaining a rather continuous shadow contrast. Analyzing all MFM contrasts for $Q = -1$ to $Q = -10$, we observe that starting at $Q = -3$, each spin object shows $|Q| - 1$ attractive lobes inside. In the case of the antiskyrmions, the shadow contrast becomes localized and leads to repulsive lobes around the boundary and Néel segments with head-to-head spin configurations, while maintaining a rather continuous attractive boundary inside the spin-object. Here, for all spin objects, we observe $|Q| + 1$ repulsive lobes. For completeness, we provide the MFM contrasts for higher-order skyrmions and antiskyrmions with $-10 \leq Q \leq 10$ in the Supporting Information.

The main goal of our paper is to experimentally investigate these qualitative MFM signatures of higher-order skyrmions. In the following, we discuss the considered samples and their magnetic characterization and imaging.

2.2 | Growth and Magnetic Characterization of Co/Ni-Multilayers

A schematic illustration of the stack of deposited layers is displayed in Figure 2a. The total stack is Si-SiOx substrate / Pt(3)/$[Co(0.2)Ni(0.7)]_8$/Co(0.2)/Ru(0.4)/Pt(5) with thicknesses given in nanometers. Within the same deposition run, we also included a 30 nm SiN membrane to be used for LTEM measurements. Magnetic hysteresis loops were measured for both oop and in-plane (ip) fields with a superconducting quantum interference device-vibrating sample magnetometer (SQUID-VSM). The $M(H)$ loops are presented in Figure 2b. The oop loop is typical for a system with perpendicular anisotropy, which is, however, too weak to keep the film in the saturated state. Hence, domains form when the field is removed. The ip loop shows hysteretic behavior for fields below 25 mT, and a non-hysteretic increase in magnetization, reaching saturation only for larger fields. We attribute this non-hysteretic part to a rotation of the magnetization into the plane for large ip fields. The hysteresis that occurs for smaller fields arises from the magnetic moments inside the domain walls that align parallel to the applied field in the plane [41].

From the same ip hysteresis curve we approximate the effective anisotropy field $\mu_0 H_k^{\text{eff}} = 118\,\text{mT}$. With a saturation magnetization $M_s = 550\,\text{kA}m^{-1}$, the perpendicular magnetic anisotropy can be calculated as $K_u = K_{\text{eff}} + \frac{1}{2}\mu_0 M_s^2$, where $K_{\text{eff}} = 32.5\,kJm^{-1}$ from $K_{\text{eff}} = \frac{1}{2}\mu_0 H_k^{\text{eff}} M_s$. Thus, we obtain $K_u = 222.4\,kJm^{-}3$. When comparing these values with the stability phase diagram of higher-order spin textures given in ref. [30], we see that our values fit inside the stability region, but in the lower left corner, where mostly antiskyrmions and very few spin textures with $|Q|$ higher than 1 should be stable.

2.3 | Lorentz Transmission Electron Microscopy of Spin Objects

To confirm that spin textures are present in our sample, we use LTEM in Fresnel mode. The LTEM contrasts are acquired at −2 mm defocus which are sensitive to the ip components of the magnetization. The background subtracted LTEM results are shown in Figure 2c–f. Figure 2c shows the zero-field multidomain states, which typically have many vBLs in the domain walls. Because of the low magnetic moment of the sample and the low nominal thickness, the obtained signals have a relatively weak contrast. Thus, background subtraction was used to increase visibility of the textures [42]. The evolution of the magnetization state with the applied oop field is shown in Figure 2d–f. With an increasing field, the domains with magnetization antiparallel to the field shrink and collapse into various types of spin textures. Figure 2g,h shows zoomed-in images of skyrmions with clockwise and counterclockwise circularities, respectively. Note that only Block skyrmions are observed in our sample, which is in agreement with previous results [30]. This behavior is supported by the lack of DMI in our stack, which is commonly required for the stabilization of Néel type of skyrmions. Furthermore, many trivial bubbles can be observed, as also exemplified in Figure 2i. Finally, a first-order antiskyrmion is shown in Figure 2j. Further uncategorized spin objects appear at low oop magnetic fields, the high defocus value of LTEM makes the discrimination of further spin objects rather challenging.

2.4 | Large Scale Micromagnetic Simulations

After the magnetic characterization, we now turn back to micromagnetic simulations to simulate a large-scaled system using measured material parameters instead of initially used material parameters; see Methods for more details. For the sake of clarity, the initial parameters were chosen to obtain stable higher-order skyrmions and antiskyrmions with arbitrary topological charges for a better understanding of their key MFM features. Note that the material parameters define the stability regime for the spin-textures. Figure 3 shows the field-dependent evolution of the magnetic states using snapshots of the oop component of the magnetization. At vanishing fields, a multidomain maze domain is observed with many single spin-objects formed and a high number of vBLs. Upon increasing the positive oop fields, the negative domains (blue) start to shrink, and smaller domains and isolated spin objects are observed, which appear to have a rather irregular shape caused by the nonhomogeneity of material parameters.

The MFM contrasts are obtained from these magnetic states using the same parameters as before at a simulated sample-to-tip distance of 30 nm. At vanishing fields, a series of localized red and blue lobes are observed at the inner (outer) boundaries of the domains. These are vBLs that lead to head-to-head and tail-to-tail spin configurations in an alternating order. Furthermore, many (randomly distributed) individual spin objects appear at vanishing fields, which show the key features of higher-order skyrmions and antiskyrmions. Their irregular shapes are now clearer as the red/blue lobes are not uniformly spaced, but can be sparsely distributed on the boundaries.

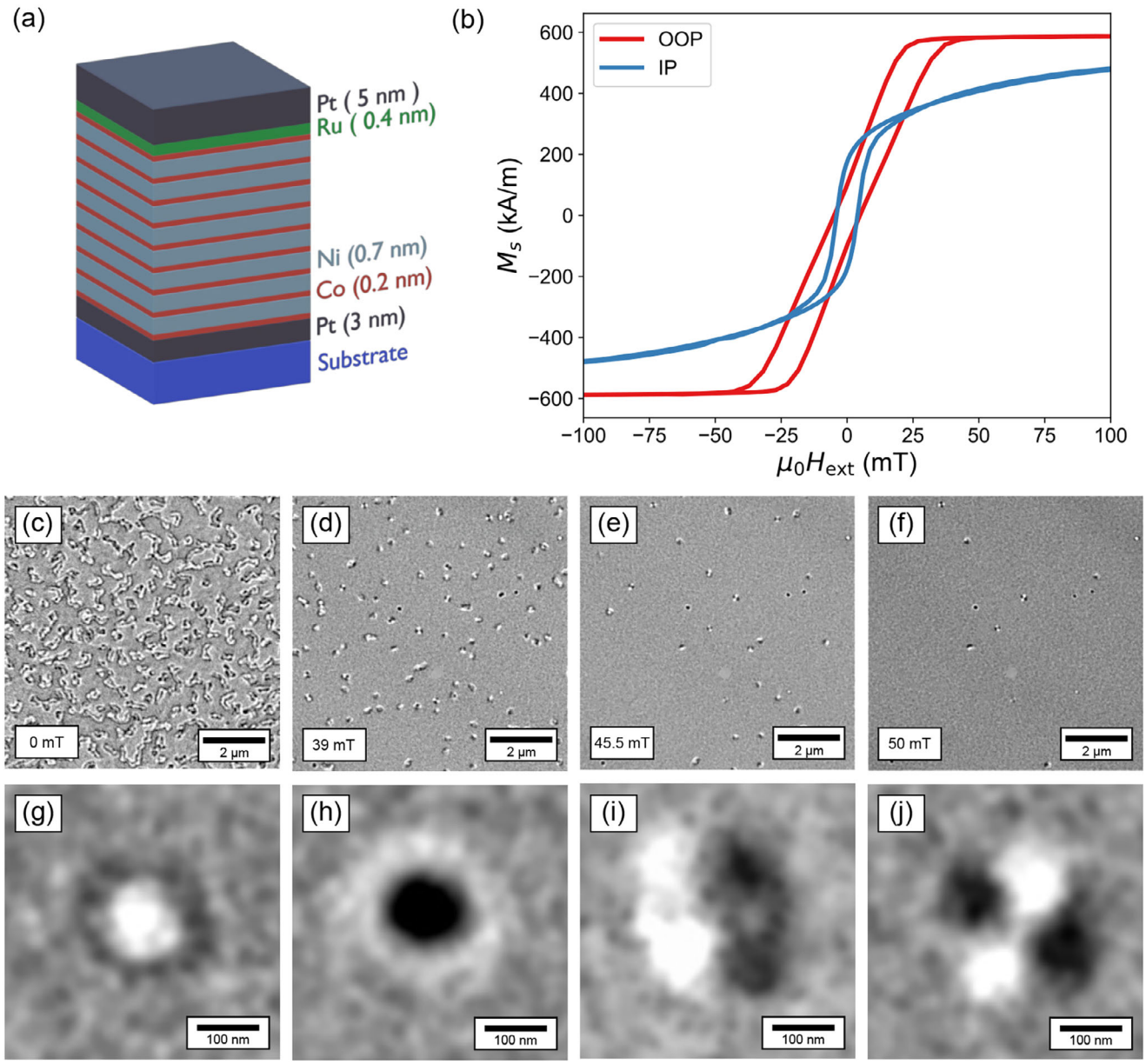

FIGURE 2 | Experimental magnetic characterization and LTEM imaging. (a) Schematic illustration of the investigated magnetic multilayer stack: Si-SiOx/ Pt(3)/ $[Co(0.2)Ni(0.7)]_{x8}$/Co(0.2)/Ru(0.4)/Pt(5) (thicknesses in nanometer). (b) $M(H)$ hysteresis loops of the sample measured for both oop (red) and ip (blue) directions. LTEM micrographs taken at room temperature at an external oop field of (c) 0 mT, (d) 39 mT, (e) 45.5 mT, and (f) 50 mT with samples grown on 30 nm Si_3N_4 membranes. Zoomed in images of an isolated (g) clockwise and (h) counterclockwise skyrmion, (i) a trivial type-II bubble, and (j) an antiskyrmion.

When the magnetic field is further increased, we observe that many of the spin objects that were originally found at vanishing fields are now annihilated. However, new spin textures form from domains with vBLs and remain stable until their further annihilation by very strong oop fields. Furthermore, we observe that irregular objects can rearrange themselves into more ordered and circular spin objects with uniformly spaced red/blue lobes. Based on our knowledge about the contrasts of individual spin objects, we can recognize that we have a plethora of spin objects with arbitrary topological charges, which we will consider in more detail later. Note that the noisy background in the figures is caused by the introduction of a grain-wise distributed anisotropy axis following a random anisotropy model [43].

2.5 | Experimental MFM of Higher-Order Spin Textures

To verify if we can experimentally discriminate between the spin objects, as numerically demonstrated, we use a home-built MFM operated under vacuum conditions.

Similarly to LTEM, and our micromagnetic modeling, MFM also picks up a magnetic background contrast arising from local variations of the magnetic moment areal density, from the c-axis variations of the crystalline grains away from the normal axis. Additionally, scanning at constant average height leads to a local variation of the van der Waals force (derivative) arising from the

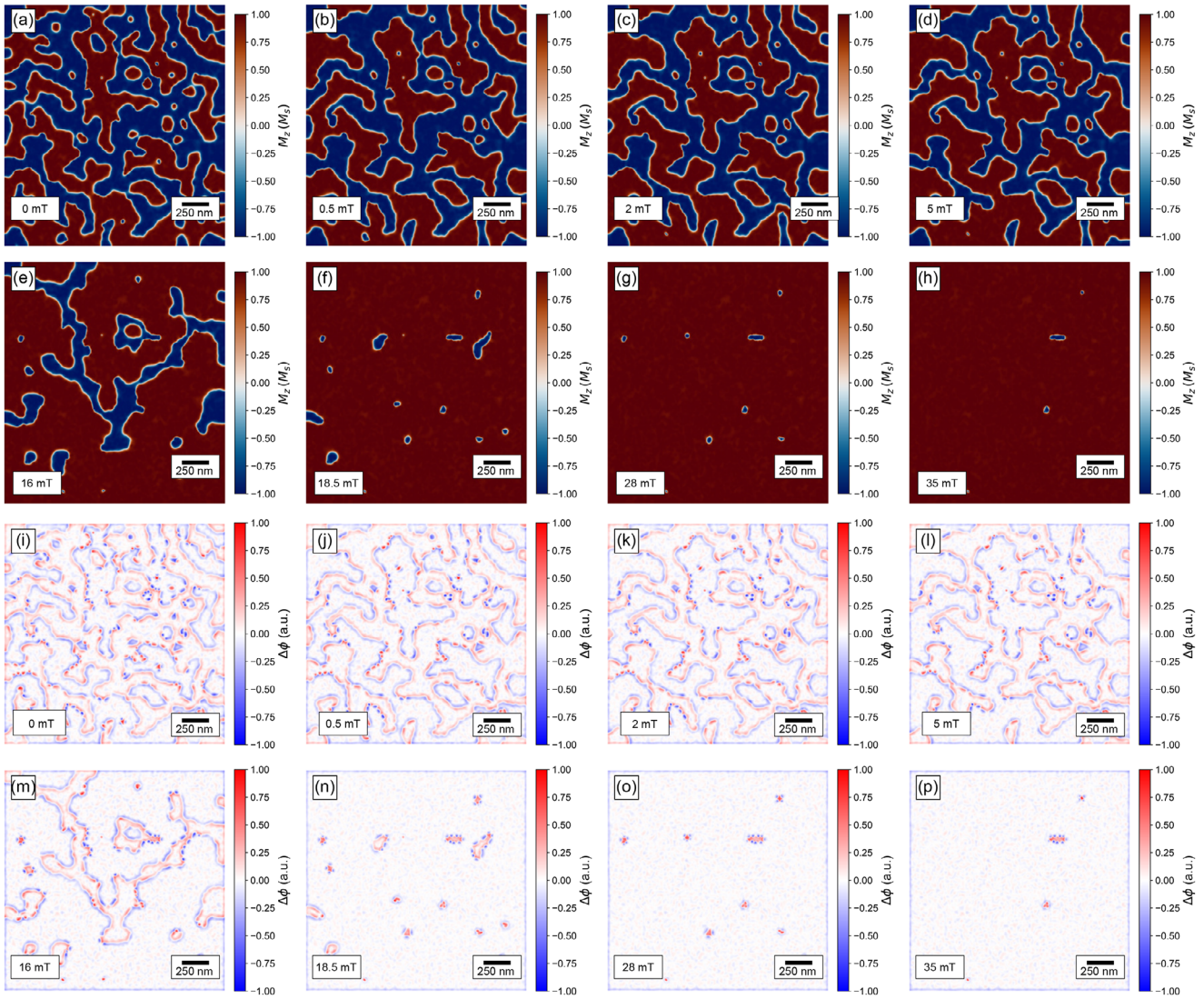

FIGURE 3 | Evolution of the microstates revealed by simulations. Micromagnetic simulations using measured material parameters, where in the field-driven evolution of the magnetic states is illustrated as the normalized oop component of the magnetization (M_z/M_s) as shown in (a)–(h), and the corresponding MFM contrasts as shown in (i)–(p), where the color represents the normalized phase shift $\Delta\phi$.

(small) sample topography. Subtraction of MFM data obtained with the sample in a saturated state from data measured at smaller fields removes these background contrast contributions, making the small spin textures of the sample more visible.

In addition to main contrast forming mechanisms, the cantilever normal is canted by 12° relative to the surface normal (which is typical for all scanning force microscopy setups) and, in our case, aligned along the y axis of the images shown in this work. The oscillation of the cantilever along this canted axis then leads to a noticeable asymmetry of the domain walls along the image y axis [39]. Because the MFM maps the stray field and not the magnetization, such domain wall asymmetries may impose challenges when different spin textures need to be distinguished.

Figure 4 presents MFM data for which the background measured in saturation and the domain wall asymmetries arising from the canted oscillation of the cantilever have been removed, together with a part of the distance loss [39]. For comparison, an unprocessed MFM image at 0 mT is provided in Figure S1. To enhance the contrast arising from such variations of the small spatial wavelengths, components of the spin texture, and consequently of the stray-field, high-pass filtering is employed (for further details on the high-pass filtering, see Section S1). More information on this process is given in Sections S1 and S2. Note that a careful post-processing of the data is crucial to reveal the key signatures of different spin objects.

In good agreement to the LTEM data (Figure 2) and the micromagnetic simulations (Figure 3), the MFM data in Figure 4 reveals submicrometer domain structures under zero field conditions, characterized by domain walls that exhibit various acute bends and kinks attributable to the presence of vBLs (Figure 4a). The up domains become smaller and sparser when increasing the field up to 20 mT. Between 25 and 35 mT smaller domains, circular and elliptical spin textures form (Figure 4f–h), while at 45 mT only a few spin textures with sub-100nm diameter are visible (Figure 4j). Note that the horizontal lines visible at some

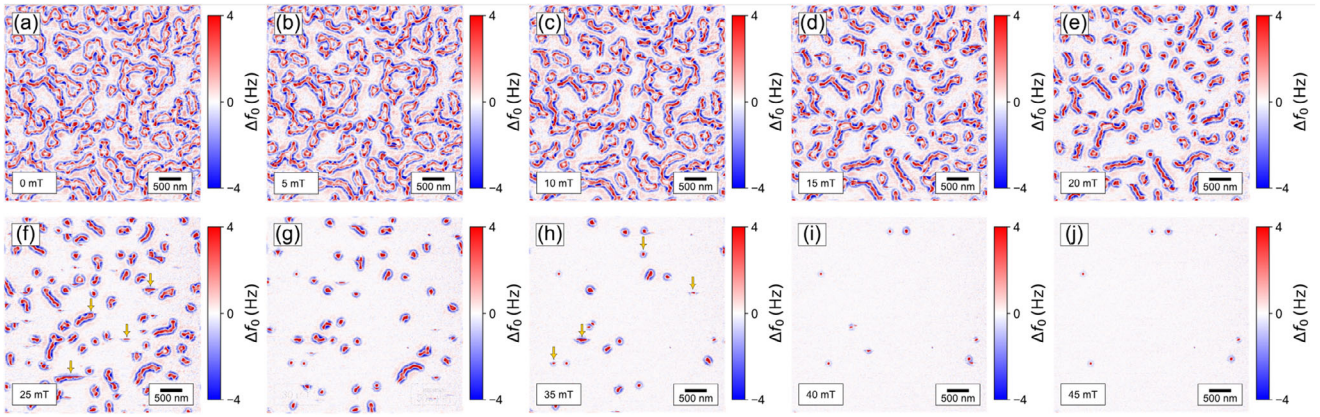

FIGURE 4 | Experimental MFM data. Post-processed data after background substraction and removing distortion arising from the cantilever canting. The data represents the measured frequency shifts under different oop fields ranging from (a) 0 mT and (j) 45 mT. A highpass filter is applied to the images to better highlight the frequency shift originating from the local stray fields, as explained in greater detail in the Supporting Information. The yellow arrows indicate scan lines where a sudden relaxation of the micromagnetic structure during scanning was observed.

locations (see yellow arrows in panels (h)) arise from a sudden evolution of the micromagnetic structure (Barkhausen jump) possibly triggered by the stray field of the scanning MFM tip.

The discrimination of these spin textures from MFM images arising from the stray field (derivative) remains more challenging and requires their corroboration to micromagnetic simulations. This is because the stray field is dominated by the up/down area of the spin texture, whereas the vBLs only lead to a weak, very local stray field modification at the domain wall. Thus, it was important to establish the key features to look for (e.g., by micromagnetic simulations) in order to identify the spin objects. For clarity, we would like to stress out that a direct quantification of the topological charge from the acquired MFM data might be possible by a quantitative reconstruction of magnetization, which is rather challenging. Instead, we corroborate our experimental results with the key features obtained from micromagnetic simulations.

In the following, we isolated special cases that we have observed in our MFM experiments, and displayed them in Figure 5. For a full confirmation, we corroborate our experimental data with simulated MFM contrasts and magnetization states obtained from micromagnetic simulations presented in Section 2.4.

In Figure 5a the MFM data of the small domains is depicted, which was acquired at 0 mT. Typically, the MFM contrast of a domain wall separating up- and down-domains highlights the localized stray field at the domain wall location. Thus, a simple blue and red adjacent contrasts are expected. In contrast, we observe in Figure 5a that the blue dots are enclosed within the domain wall by white rings. Compared with the MFM contrasts from the middle panel, which is calculated from the magnetization pattern shown in the right panel, it becomes obvious that the blue spots indicated with yellow arrows in (a,b) are vBLs.

The data displayed in Figure 5b shows a skyrmion characterized by its perfectly circular symmetry with the dark blue shadow contrast arising from the return of the magnetic flux, as discussed in Section 2.1. From the comparison to MFM simulations and magnetization snapshot, we can see that we can classify this object as a skyrmion. In contrast to Néel walls, Bloch walls, however, do not generate a magnetic volume charge density, and thus Bloch skyrmions with different wall chiralities generate the same stray field and cannot thus be distinguished by MFM or any microscopy method that maps the stray field above the sample. Note that for skyrmions with Néel walls, the additional volume magnetic charge density arising from the divergence of the magnetization field in the Néel walls either amplifies or attenuates the skyrmion stray field, making it possible to distinguish counterclockwise and clockwise Néel skyrmions, respectively, from a quantiative analysis of the stray field [44, 45]. In contrast, different Bloch wall chiralities lead to a very different appearance of the skyrmions in LTEM images (compare Figure 2g,h). Nevertheless, here it becomes obvious that the shadow contrast around the spin objects can be measured and is a key signature for the skyrmion, as discussed in previous sections. The shadow ring is also present in the spin objects presented in Figure 5 cd, where in the former two red MFM contrasts are visible, while the overall shape corresponds to two merged skyrmions. Compared to the micromagnetic simulations in the middle and right panels, we can identify this spin texture as a $Q = -2$ biskyrmion. The small defect highlighted in gray dashed circle might originate either from an actual topological defect or is a consequence of local pinning. The MFM simulations reveal a similar shape where the pinning leads to an asymmetric signal with a strong background noise. Counting the red lobes inside of the image in Figure 5d indicates that we have imaged a $Q = -4$ higher-order skyrmion, which is further corroborated by the simulated MFM contrasts from the middle pannel and confirmed by the magnetization configuration from the right panel. Again, the imperfections slightly modify the perfect symmetrical shape we showed in the overview presented in the Supporting Information.

Another very distinct shape that we have imaged experimentally appears in Figure 5e, where the shadow contrast is interupted on one side and has the crescent form we discussed earlier, which indicates that this spin object is a trivial bubble. While this spin-object was not visible from the large-scale simulations shown in Section 2.4, we decided to provide the MFM and magnetization contrast of a parametrized and relaxed spin object, as we have done in Section 2.4. Here, it is also noteworthy, that comparing the

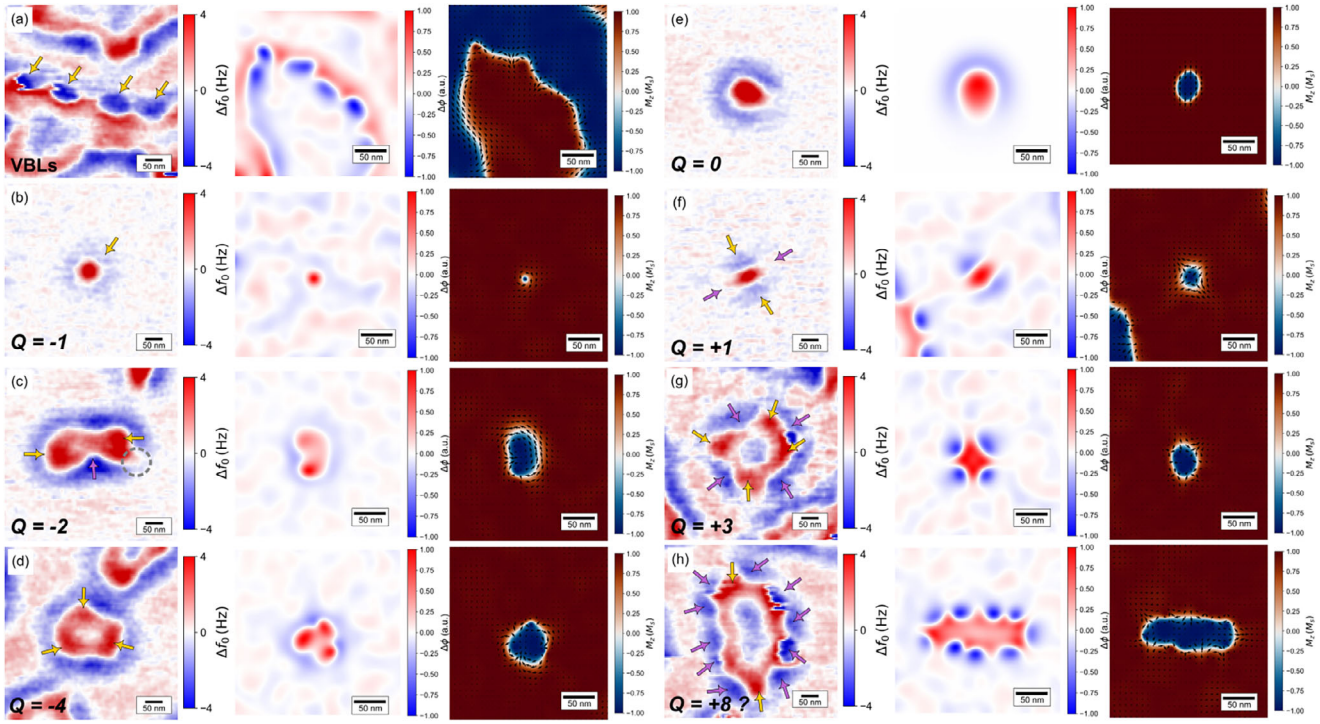

FIGURE 5 | Comparison of experimental and simulated contrasts of single objects. Isolated experimental MFM images are shown in the upper pannel of (a)–(g) with vBLs in (a), a $Q = -1$ skyrmion in (b), a $Q = -2$ (bi)skyrmion in (c), a $Q = -4$ higher-order skyrmion in (d), a $Q = +1$ antiskyrmion in (e), a $Q = +3$ higher-order antiskyrmion in (f), and a higher-order antiskyrmion with $Q = +10$ in (q). The yellow arrows in (a) show the location of vBLs and the high strayfield contrasts sourcing from the kinks of the domain boundary of higher order spin objects. For comparison purposes, corresponding simulated MFM contrasts (middle panel) and M_z/M_s component of the magnetization (lower panel) are shown.

experimentally acquired contrasts of the biskyrmion in Figure 5c and of the trivial bubble in Figure 5e have clearly different signatures. Hence, this confirms our initial numerical predictions that the MFM signatures of spin objects are rather unique.

Further, the spin object displayed in Figure 5f has a noticeably different appearance with its slightly elliptical shape and two blue shadow contrasts opposing each other, in perfect agreement to the MFM contrast of an antiskyrmion we discussed before. Here, we confirm by experiments that the MFM contrast of an antiskyrmion has a different signature regarding its magnetic flux shadow ring: instead of a circular core and continuous ring, the antiskyrmions' contrast is distinguished by an elliptical core and the presence of two blue lobes located at the top and bottom (yellow arrows). An important observation is that a counterclockwise wall structure (head-to-head, yellow arrows in Figure 5f amplifies the stray field at the top and bottom of the antiskyrmion spin texture leading to a sharp and pronounced stray field contribution, whereas the clockwise wall structure (tail-to-tail, purple arrows) lead to a decrease in contrast.

Panels (g) and (h) of Figure 5 further show higher-order antiskyrmions with topological charge $Q = +3$ and possibly $Q \geq 8$. In Section 2.1, we pointed out that with increasing topological charge, the radius of the (anti)skyrmions will also increase. Thus, the core becomes more uniformly magnetized compared to the domain wall boundaries. The resulting stray field and the corresponding MFM contrast is expected to weaken in the core itself, a phenomenon that we can now also observe experimentally. In panel (g), the contrast in the domain wall is particularly pronounced, with the four dark red lobes marked by purple arrows and blue lobes marked by yellow arrows. By quantifying the number of red and blue lobes, we can identify the spin object in panel (g) with considerable confidence as $Q = 4$. In contrast, the texture observed in panel (h) presents greater challenges in assessment and classification with a similar degree of certainty. Compared with the MFM contrasts of an antiskyrmion $Q = 8$, it is possible that the texture in (h) has a charge higher than $Q = 8$. Nevertheless, the key features are still represented in a spin object with a high topological charge. A direct quantification of the topological charge can be achieved by a 3D reconstruction of the magnetization by means of tomographic imaging techniques [36].

3 | Conclusions

In conclusion, we demonstrated that skyrmions, trivial bubbles, and antiskyrmions of different topological charges present in Co/Ni multilayers can be imaged and distinguished by MFM. MFM does not directly image the local magnetization texture, but rather the stray field (derivative) generated by divergences (magnetic charges) of the magnetization. While the positive and negative magnetic surface charges appearing at the top and bottom surfaces are the dominant sources for the stray field, the magnetic volume charges arising from local Néel wall type spin textures lead to modulations of the wall contrast that can be made visible by MFM techniques and permit distinguishing between different types of spin textures. Our results demonstrate that MFM is a viable technique to image and discriminate spin textures with different topological charges. As predicted numerically in our

earlier work [30], the spin textures with higher topological charge might move with a reduced skyrmion Hall effect, and opposing charges lead to opposing lateral deflections. As MFM enables one to study the current-driven transport properties of spin textures such as skyrmions [46], we are confident that our results will have an impact on the future investigation of higher-order skyrmions and antiskyrmions, especially for their prototypical usage in possible memory and computing applications.

4 | Experimental Section

4.1 | Sample Fabrication

A Co/Ni multilayer thin film was deposited via magnetron sputtering at room temperature on a Si(100)-SiOx substrate. The base pressure inside the ultrahigh vacuum chamber was below 1×10^{-8} mbar. The materials were DC magnetron sputtered from elemental targets utilizing Ar gas at a sputter pressure of 3.5 mbar. A 5 nm Pt layer was used as a capping layer.

4.2 | Lorentz Transmission Electron Microscopy

A JEOL NEOARM-200F transmission electron microscope was operated at an acceleration voltage of 200 keV in Fresnel mode to acquire images of the magnetization states under different oop fields, utilizing 2 mm underfocus. The images were acquired with a Gatan OneView camera. Background subtraction was applied to improve the visibility of the spin textures [42].

4.3 | Magnetic Force Microscopy

To maximize the signal-to-noise ratio and spatial resolution, a team Nanotec SS-ISC uncoated cantilever was employed with a tip radius smaller than 5 nm, a (measured) resonance frequency of 55.859 kHz and a force constant of 1.16 Nm^{-1} calculated from the length of the cantilever ($225\mu m$), width ($35\mu m$) and resonance frequency. The tip was made sensitive to magnetic stray fields by coating a Ta(2 nm)/Co(4.5 nm)/Ta(3 nm) film on the top side of the tip facing the cantilever chip. Magnetic layer deposition was performed with a mask to avoid coating the cantilever toward its attachment point to the chip to obtain a high quality factor $Q = 150 \times 10^3$ [39]. The cantilever was then driven on resonance by a phase-looked loop at an oscillation amplitude $A = 5$ nm. The measured signal was a shift of the resonance frequency, Δf, while the phase remains locked at -90°. Moreover, an attractive magnetic force (derivative) occuring for example from the stray field of an up domain imaged by an up-magnetized tip then leads to a negative frequency shift, here depicted with blue color. A single-passage scan mode was used where the tip-sample distance is controlled by a frequency-modulated capacitive feedback as described in an earlier work [47]. With this operation mode, the tip never makes contact with the sample, and hence did not wear. A tip sample distance of 10 nm was kept constant on average and did not follow the local topography, with a precision of more than 0.5 nm for many days and for different applied magnetic fields. This permits differential imaging techniques, for example, to subtract a background, i.e., the MFM data obtained in saturation from data measured at different fields (see Section S1).

4.4 | Micromagnetic Simulations

4.4.1 | Isolated Objects

We used a simulation box with (256x256x1) cells with a discretization length of (1 nm × 1 nm × 5 nm). We know from ref. [30] that a finer discretization along z only lead to negligible differences and the quasi-2D approximation used here is valid. For material parameters, we chose $M_s = 940$ kA/m, $A_{ex} = 10$ pJm^{-1}, and $K_u = 575$ kJm^{-3} as in ref. [30], where we know that spin objects with arbitrary spin textures are stable. Skyrmions and antiskyrmions of arbitrary orders are initialized by a rough parameterization and later relaxed under an oop field by numerically integrating the Landau-Lifshitz-Gilbert equation at high damping $\alpha = 1.0$ for 10 ns. The MFM contrast was calculated following the approach used by Holt et al. [48], where the phase shift $\Delta\phi$ is defined as:

$$\Delta\phi = \frac{q\mu_0}{k}\left(\boldsymbol{\mu}_{tip} \cdot \frac{\partial^2 \mathbf{H}_z}{\partial z^2}\right) \tag{1}$$

where q describes the quality factor and k the spring constant of the cantilever, μ_0 is the vacuum permeability. $\boldsymbol{\mu}_{\text{tip}}$ denotes the effective dipole moment of the tip and $\mathbf{H}_z$ denotes the oop component of the stray field at a chosen height. For simplicity, we use $q = 1$ and $k = 1$. The moment of tip is chosen as $\boldsymbol{\mu}_{\text{tip}} = (0, 0, \pm 1 \times 10^{-16}\ \text{Am}^{-2})$.

4.4.2 | Large-Scale Simulations

We discretize a box into ($2048 \times 2048 \times 1$) cells with dimensions (1 nm × 1 nm × 7.4 nm). To simulate the expected granular polycrystallinity of the sample, we used a voronoi tessellation with an average grain size of approximately 15 nm. The average material parameters were $\langle M_s \rangle = 550\, kAm^{-1}$, $\langle A_{\text{ex}} \rangle = 10\, pJm^{-1}$, $\langle K_u \rangle = 222$ kJm^{-3}. The scalar parameters were then varied grainwise with a normal distribution with a standard deviation of 5% of the average value. Furthermore, the anisotropy axis was distributed (grainwise) uniformly on a cone around the oop axis, with a maximum deviation of 5°. This allows us to create nucleation and pinning sites that were relevant for the nucleation of spin objects. The total energy of the system includes the demagnetization, exchange, anisotropy, as well as Zeeman energies. For the latter, the oop magnetic field was varied in 1 mT steps from 0 to 50 mT. The magnetization was initially relaxed from a random state by using an energy minimizer to speed up the computations [40], with the oop field increasing after each relaxation process.

Acknowledgments

S.K. and D.S. acknowledge funding from the Austrian Science Fund (FWF) under grant no. I6267 (CHIRALSPIN). S.K. thanks the Vienna Doctoral School in Physics for funding the Mobility Fellowship. S.K. acknowledges funding from the European Research Council (ERC) under the European Union's Horizon 2020 research and innovation programme, grant agreement no. 101001290 (3DNANOMAG). The authors acknowledge Vienna Scientific Cluster for awarding this project access to the LEONARDO supercomputer, owned by the EuroHPC Joint Undertaking, hosted by CINECA (Italy) and the LEONARDO consortium. T.K. and F.B. acknowledged funding by the Helmholtz Young Investigator Group

Program through project VH-NG-1520 and by the DFG through projects 462676630 (BU 3297/3-1) and 49254781 (TRR-360, sub-project C02). M.A. gratefully acknowledges funding from Deutsche Forschungsgemeinschaft (DFG, German Research Foundation) grant no. 507821284. J.S. acknowledges financial support and a scholarship received from the Bavarian Research Foundation (DOK-193-22).

Open Access funding provided by Technische Universitat Wien/KEMö.

Conflicts of Interest

The authors declare no conflicts of interest.

Data Availability Statement

The data that support the findings of this study are available from the corresponding author upon reasonable request.

References

1. D. Suess, A. Bachleitner-Hofmann, A. Satz, et al., "Topologically Protected Vortex Structures for Low-Noise Magnetic Sensors with High Linear Range," *Nature Electronics* 1 (2018): 362.

2. D. C. Leitao, F. J. V. Riel, M. Rasly, et al., "Enhanced Performance and Functionality in Spintronic Sensors," *npj Spintronics* 2 (2024): 54.

3. S. S. Parkin, M. Hayashi, and L. Thomas, "Magnetic Domain-Wall Racetrack Memory," *Science* 320 (2008): 190.

4. D. A. Allwood, G. Xiong, C. Faulkner, D. Atkinson, D. Petit, and R. Cowburn, "Magnetic Domain-Wall Logic," *Science* 309 (2005): 1688.

5. Z. Luo, A. Hrabec, T. P. Dao, et al., "Current-Driven Magnetic Domain-Wall Logic," *Nature* 579 (2020): 214.

6. D. Kumar, T. Jin, R. Sbiaa, et al., "Domain Wall Memory: Physics, Materials, and Devices," *Physics Reports* 958 (2022): 1.

7. G. Catalan, J. Seidel, R. Ramesh, and J. F. Scott, "Domain Wall Nanoelectronics," *Reviews of Modern Physics* 84 (2012): 119.

8. U. K. Roessler, A. Bogdanov, and C. Pfleiderer, "Spontaneous Skyrmion Ground States in Magnetic Metals," *Nature* 442 (2006): 797.

9. X. Yu, Y. Onose, N. Kanazawa, et al., "Real-Space Observation of a Two-Dimensional Skyrmion Crystal," *Nature* 465 (2010): 901.

10. A. Fert, V. Cros, and J. Sampaio, "Skyrmions on the Track," *Nature Nanotechnology* 8 (2013): 152.

11. R. Tomasello, E. Martinez, R. Zivieri, L. Torres, M. Carpentieri, and G. Finocchio, "A Strategy for the Design of Skyrmion Racetrack Memories," *Scientific Reports* 4 (2014): 1.

12. A. Fert, N. Reyren, and V. Cros, "Magnetic Skyrmions: Advances in Physics and Potential Applications," *Nature Reviews Materials* 2 (2017): 1.

13. D. Pinna, G. Bourianoff, and K. Everschor-Sitte, "Reservoir Computing with Random Skyrmion Textures," *Physical Review Applied* 14 (2020): 054020.

14. K. Raab, M. A. Brems, G. Beneke, et al., "Brownian Reservoir Computing Realized Using Geometrically Confined Skyrmion Dynamics," *Nature Communications* 13 (2022): 6982.

15. O. Lee, T. Wei, K. D. Stenning, et al., "Task-Adaptive Physical Reservoir Computing," *Nature Materials* 23 (2024): 79.

16. G. Beneke, T. B. Winkler, K. Raab, et al., "Gesture Recognition with Brownian Reservoir Computing Using Geometrically Confined Skyrmion Dynamics," *Nature Communications* 15 (2024): 8103.

17. M. Hoffmann, G. P. Müller, C. Melcher, and S. Blügel, "Skyrmion-Antiskyrmion Racetrack Memory in Rank-One DMI Materials," *Frontiers in Physics* 9 (2021): 769873.

18. A. K. Nayak, V. Kumar, T. Ma, et al., "Magnetic Antiskyrmions Above Room Temperature in Tetragonal Heusler Materials," *Nature* 548 (2017): 561.

19. L. Peng, R. Takagi, W. Koshibae, et al., "Controlled Transformation of Skyrmions and Antiskyrmions in a Non-Centrosymmetric Magnet," *Nature Nanotechnology* 15 (2020): 181.

20. J. Jena, B. Göbel, T. Ma, et al., "Elliptical Bloch Skyrmion Chiral Twins in an Antiskyrmion System," *Nature Communications* 11 (2020): 1115.

21. F. Zheng, N. S. Kiselev, L. Yang, et al., "Skyrmion–Antiskyrmion Pair Creation and Annihilation in a Cubic Chiral Magnet," *Nature Physics* 18 (2022): 863.

22. M. Heigl, S. Koraltan, M. Vaňatka, et al., "Dipolar-Stabilized First- and Second-Order Antiskyrmions in Ferrimagnetic Multilayers," *Nature Communications* 12 (2021): 2611.

23. D. Foster, C. Kind, P. J. Ackerman, J. S. B. Tai, M. R. Dennis, and I. I. Smalyukh, "Two-Dimensional Skyrmion Bags in Liquid Crystals and Ferromagnets," *Nature Physics* 15 (2019): 655.

24. J. Tang, Y. Wu, W. Wang, et al., "Magnetic Skyrmion Bundles and Their Current-Driven Dynamics," *Nature Nanotechnology* 16 (2021): 1086.

25. L. Yang, A. S. Savchenko, F. Zheng, et al., "Embedded Skyrmion Bags in Thin Films of Chiral Magnets," *Advanced Materials* 36 (2024): 2403274.

26. Y. Zhang, J. Tang, Y. Wu, et al., "Stable Skyrmion Bundles at Room Temperature and Zero Magnetic Field in a Chiral Magnet," *Nature Communications* 15 (2024): 3391.

27. A. Rosencwaig, W. J. Tabor, and T. Nelson, "New Domain-Wall Configuration for Magnetic Bubbles," *Physical Review Letters* 29 (1972): 946.

28. J. Slonczewski, A. Malozemoff, and O. Voegeli, "Statics and Dynamics of Bubbles Containing Bloch Lines," in *AIP Conference Proceedings* 10 (American Institute of Physics, 1973), 458–477.

29. P. Grundy, "Magnetic Bubbles and Their Observation in the Electron Microscope," *Contemporary Physics* 18 (1977): 47.

30. M. Hassan, S. Koraltan, A. Ullrich, et al., "Dipolar Skyrmions and Antiskyrmions of Arbitrary Topological Charge at Room Temperature," *Nature Physics* 20 (2024): 615–622.

31. X. Chen, L. Yang, A. Savchenko, et al., "Fact and Artifact in Lorentz Imaging of Skyrmionic Magnetic Textures," *Physical Review B* 112 (2025): 214455.

32. X. Yu, Y. Tokunaga, Y. Kaneko, et al., "Biskyrmion States and Their Current-Driven Motion in a Layered Manganite," *Nature Communications* 5 (2014): 3198.

33. W. Wang, Y. Zhang, G. Xu, et al., "A Centrosymmetric Hexagonal Magnet with Superstable Biskyrmion Magnetic Nanodomains in a Wide Temperature Range of 100–340 K," *Advanced Materials* 28 (2016): 6887.

34. J. T. Lee, J. Chess, S. Montoya, et al., "Synthesizing Skyrmion Bound Pairs in Fe-Gd Thin Films," *Applied Physics Letters* 109 (2016): 022402.

35. J. C. Loudon, A. C. Twitchett-Harrison, and D. Cortés-Ortuño, "Do Images of Biskyrmions Show Type-II Bubbles?," *Advanced Materials* 31 (2019): 1806598.

36. D. Raftrey, S. Finizio, R. V. Chopdekar, et al., "Quantifying the Topology of Magnetic Skyrmions in Three Dimensions," *Science Advances* 10 (2024): eadp8615.

37. M. Di Pietro Martínez, A. Wartelle, C. Herrero Martínez, et al., "Three-Dimensional Tomographic Imaging of the Magnetization Vector Field Using Fourier Transform Holography," *Physical Review B* 107 (2023): 094425.

38. Y. Dovzhenko, F. Casola, S. Schlotter, et al., "Magnetostatic Twists in Room-Temperature Skyrmions Explored by Nitrogen-Vacancy Center Spin Texture Reconstruction," *Nature Communications* 9 (2018): 2712.

39. Y. Feng, P. M. Vaghefi, S. Vranjkovic, et al., "Magnetic Force Microscopy Contrast Formation and Field Sensitivity," *Journal of Magnetism and Magnetic Materials* 551 (2022): 169073.

40. F. Bruckner, S. Koraltan, C. Abert, and D. Suess, "Magnum.NP: A PyTorch-Based GPU-Enhanced Finite-Difference Micromagnetic

Simulation Framework for High-Level Development and Inverse Design," *Scientific Reports* 13 (2023): 12054.

41. M. A. Marioni, N. Pilet, T. V. Ashworth, R. C. O'Handley, and H. J. Hug, "Remanence Due to Wall Magnetization and Counterintuitive Magnetometry Data in 200-nm Films of Ni," *Physical Review Letters* 97 (2006): 027201.

42. T. Denneulin, J. Caron, K. Múller-Caspary, O. Boulle, A. Kovács, and R. E. Dunin-Borkowski, "Visibility and Apparent Size of Néel-Type Magnetic Skyrmions in Fresnel Defocus Images of Multilayer Films," *Microscopy and Microanalysis* 27 (2021): 1356.

43. A. Kákay and L. Varga, "Micromagnetic Simulation of Random Anisotropy Model," *Journal of Magnetism and Magnetic Materials* 272 (2004): 741.

44. M. A. Marioni, M. Penedo, M. Bacani, J. Schwenk, and H. J. Hug, "Halbach Effect at the Nanoscale from Chiral Spin Textures," *Nano Letters* 18 (2018): 2263.

45. M. Bacani, M. A. Marioni, J. Schwenk, and H. J. Hug, "How to Measure the Local Dzyaloshinskii-Moriya Interaction in Skyrmion Thin-Film Multilayers," *Scientific Reports* 9 (2019): 3114.

46. V. T. Pham, N. Sisodia, I. Di Manici, et al., "Fast Current-Induced Skyrmion Motion in Synthetic Antiferromagnets," *Science* 384 (2024): 307.

47. X. Zhao, J. Schwenk, A. O. Mandru, et al., "Magnetic Force Microscopy with Frequency-Modulated Capacitive Tip–Sample Distance Control," *New Journal of Physics* 20 (2018): 013018.

48. S. J. Holt, M. Lang, J. C. Loudon, et al., "Virtual Experiments in Computational Magnetism with Mag2Exp," *npj Computational Materials* 11 (2025): 201.

Supporting Information

Additional supporting information can be found online in the Supporting Information section.

Supporting File: adfm74690-sup-0001-SuppMat.pdf.